This is the pre-peer reviewed version of the following article:

Pesquera D., Parsonnet E., Qualls A., Xu R., Gubser A.J., Kim J., Jiang Y., Velarde G., Huang Y.-L., Hwang H.Y., Ramesh R., Martin L.W.. Beyond Substrates: Strain Engineering of Ferroelectric Membranes. Advanced Materials, (2020). . : - . 10.1002/adma.202003780,

which has been published in final form at https://dx.doi.org/10.1002/adma.202003780. This article may be used for non-commercial purposes in accordance with Wiley Terms and Conditions for Use of Self-Archived Versions.

Beyond Substrates: Strain Engineering of Ferroelectric Membranes

David Pesquera, Eric Parsonnet, Alexander Qualls, Ruijuan Xu, Andrew J. Gubser, Jieun Kim, Yizhe Jiang, Gabriel Velarde, Yen-Lin Huang, Harold Y. Hwang, Ramamoorthy Ramesh, and Lane W. Martin**

Dr. D. Pesquera, J. Kim, Y. Jiang, G. Velarde, Dr. Y.-L. Huang, Prof. R. Ramesh, Prof. L. W. Martin

Department of Materials Science and Engineering, University of California, Berkeley, 94720, USA

E-mail: dpesquera@cantab.net; lwmartin@berkeley.edu

Dr. D. Pesquera

Catalan Institute of Nanoscience and Nanotechnology (ICN2), CSIC and BIST, Campus UAB, Bellaterra, 08193 Barcelona, Spain

E. Parsonnet, A. Qualls, Prof. R. Ramesh

Department of Physics, University of California, Berkeley, 94720, USA

Dr. R. Xu, Prof. H. Y. Hwang

Department of Applied Physics, Stanford University, Stanford, California 94305, USA

Stanford Institute for Materials and Energy Sciences, SLAC National Accelerator Laboratory, Menlo Park, California 94025, USA

A. J. Gubser

Department of Nuclear Engineering, University of California, Berkeley, 94720, USA

Prof. R. Ramesh, Prof. L. W. Martin

Materials Sciences Division, Lawrence Berkeley National Laboratory, Berkeley, 94720, USA

Abstract

Strain engineering in perovskite oxides provides for dramatic control over material structure, phase, and properties, but is limited by the scarcity of high-quality substrates. Here, using the ferroelectric $BaTiO_3$, production of precisely strain-engineered, substrate-released nanoscale membranes is demonstrated via an epitaxial lift-off process that allows us to replicate the high

crystalline quality of films grown on substrates. In turn, fine structural tuning is achieved using interlayer stress in symmetric tri-layer oxide-metal/ferroelectric/oxide-metal structures fabricated from the released membranes. In devices integrated on silicon, the interlayer stress provides deterministic control of ordering temperature (from 75°C to 425°C) and releasing the substrate clamping is shown to dramatically impact ferroelectric switching and domain dynamics (including reducing coercive fields to < 10 kV cm^{-1} and improving switching times to < 5 ns for a 20 μm diameter capacitor in a 100-nm-thick film). In devices integrated on flexible polymers, enhanced room-temperature dielectric permittivity with large mechanical tunability (90% change upon ±0.1% strain application) is demonstrated. This approach paves the way towards the fabrication of ultrafast CMOS-compatible ferroelectric memories and ultrasensitive flexible nanosensor devices, and it may also be leveraged for the stabilization of novel phases and functionalities not achievable via direct epitaxial growth.

Perovskite ABO_3 oxides can display an immense number of phases and functions by merely changing the *A*- and *B*-site cations. Even within a single chemistry, multiple phases can be in competition, and their stability can be tuned *statically* by fixing lattice distortions in epitaxial films or *dynamically* by applying stress or external fields. Integrating the diverse functionalities of complex oxides into semiconductor and flexible electronics is a major technological challenge that has motivated extensive work on the epitaxial growth of oxide films on silicon and other semiconductors[1–7] as well as on flexible substrates.[8–12] Despite considerable effort, the structural, chemical, and thermal mismatches between such substrates and the complex-oxide materials often yield films with crystal quality considerably worse than that attained on single-crystal perovskite substrates. Alternative strategies for hetero-integration via substrate release

and transfer, mimicking the fabrication processes of van-der-Waals heterostructures,[13–15] are just now beginning to yield single-crystal oxide films on arbitrary substrates,[16–21] thus circumventing the constraints of epitaxial growth. Moreover, these detached films no longer experience mechanical constraint from the substrate, giving more flexibility in structural manipulation and heterostructure assembly.

Strain control over the lattice structure is particularly impactful in ferroelectrics where the polarization is directly connected to structural distortions.[22,23] In thin films, strain can define the optimal operating temperature regime[24–26] or domain configuration[27–29] that will boost electro-mechanical or thermal functionalities, whose associated susceptibilities (piezo-/pyroelectricity) are enhanced at temperatures near phase transitions[30] or when competing microstructures coexist.[31–34] While strain is typically introduced by substrate selection in epitaxial films, films released from the substrate relax their lattice towards their bulk crystal structure; therefore, different approaches to manipulate properties determined by structure need to be developed. Mechanical and electric-field manipulation of micron-sized freestanding flakes in electron-microscopy experiments,[35,36] as well as straining experiments on polymer-supported ultrathin perovskite membranes (restricted to films <10 nm in thickness)[37,38] have demonstrated their exceptional flexibility. Whereas transfer to polymers or electroactive substrates has been exploited to tune magnetic properties[38–40] or to test the resilience of ferroelectric properties,[41–43] strain control of properties has not been demonstrated on single-crystal ferroelectric membranes.

Mechanical separation of a film from the substrate is also expected to facilitate polarization switching processes, either by enabling ferroelastic events limited by substrate constraint,[44] or by reducing domain-wall pinning at the substrate/film interface[45]. Structural

inhomogeneities emerging in unclamped membranes, however, can mask the impact of the substrate release on the switching kinetics.[46] Therefore, preserving high crystal quality in the ferroelectric membranes after the release is important to identify intrinsic changes in switching mechanisms and domain-wall mobilities with the aim of lowering switching times, as is highly sought after for ultra-high speed, non-volatile memories,[47] memristors,[48] and neuromorphic networks.[49]

Here, we demonstrate that high-quality nanoscale epitaxial films of the prototypical ferroelectric $BaTiO_3$ (and strontium alloyed versions) can be transferred from single-crystal oxide substrates to silicon and polymer substrates avoiding structural degradation. We design a strategy to control the lattice distortion of tri-layer membranes (*i.e.*, oxide-metal electrode $Ba_{1-y}Sr_yRuO_3$ / ferroelectric $Ba_{1-x}Sr_xTiO_3$ / oxide-metal electrode $Ba_{1-y}Sr_yRuO_3$) whereby we can tailor the structure, critical temperature, polarization, and switching voltage and speed over a wide range. The ferroelectric membranes display faster switching kinetics upon release, resulting from modified domain-wall dynamics, with switching times of just a few nanoseconds upon application of low-voltage pulses. Finally, we apply heterostructure design to fabricate $Ba_{1-x}Sr_xTiO_3$ ferroelectric capacitors showing high dielectric susceptibility at room temperature and integrate them on flexible polymer substrates to obtain large strain-induced charges in dielectric permittivity (~90% with just ±0.1% strain) controlled by the substrate curvature. This work demonstrates the versatility of film transfer as a means to integrate oxide functionalities designed *ad hoc* into any technological platform.

We focus on (001)-oriented $BaTiO_3$ films (100 nm) and symmetric heterostructures of the form $Ba_{1-y}Sr_yRuO_3$ (y = 1 or 0.5; oxide-metal electrode (E) with thickness t_E = 10-40 nm) / $Ba_{1-x}Sr_xTiO_3$ (x = 0 or 0.2; ferroelectric (FE) with thickness t_{FE} = 100 nm) / $Ba_{1-y}Sr_yRuO_3$ (y = 1 or

0.5; oxide-metal electrode (E) with thickness t_E = 10-40 nm) grown on $GdScO_3$ (110) substrates buffered with 7 nm of $La_{0.7}Sr_{0.3}MnO_{3-\delta}$ produced via pulsed-laser deposition (Experimental Section). As a shorthand notation, we will refer to these symmetric tri-layer heterostructures using the form (*x*, *y*, *z*) where *x* and *y* denote the chemistry of the $Ba_{1-x}Sr_xTiO_3$ and $Ba_{1-y}Sr_yRuO_3$ layers and $z = 2t_E/t_{FE}$ refers to the thickness ratio of the different layers and t_{FE} = 100 nm for all heterostructures reported herein. The $La_{0.7}Sr_{0.3}MnO_{3-\delta}$ layer serves as an epitaxial, sacrificial-release layer that maintains the high-quality of the heterostructure, but allows for complete release of the symmetric tri-layers upon immersing the samples in an acidic solution (Experimental Section and Figure S1, Supporting Information). The etching process was found to be highly selective to the sacrificial layer and millimeter-size membranes with few or no visible cracks could be repeatably synthesized (Figure S2, Supporting Information). Following growth, these membranes were then transferred to either rigid silicon or flexible polyethylene terephthalate (PET) substrates (**Figure 1**a, Experimental Section, and Supporting Information).

X-ray diffraction line scans on a (0, 1, 0.8) heterostructure both before and after release show that the diffraction intensities and peak widths of both the ferroelectric and electrode layers remain virtually unaltered, and the 2θ position of the $BaTiO_3$ peak remains shifted with respect to the expected bulk value after the transfer of the film from the $GdScO_3$ substrate to the platinum-coated silicon (two top scans, Figure 1b), indicating that the crystallinity of all the layers is maintained and the ferroelectric layer remains strained. Moreover, Laue oscillations are still observed in the membrane even after transfer to the silicon substrate. The etching of the manganite sacrificial layer leaves no appreciable traces on the surface of the perovskite substrates (Figure S3, Supporting Information), which can then be repeatedly used as a growth template. The lattice parameters of the manganite layer can also be easily adapted via cation

doping (the pseudocubic *a* evolves from 3.73 to 3.95 Å for $CaMnO_3$[50] and $LaMnO_3$,[51] respectively) and can be further expanded via oxygen deficiency[52], allowing the use of such systems on a wide range of perovskite substrates (by contrast, the water-soluble pseudo-perovskite layers, despite also allowing lattice tunability,[19,38] have only been grown on $SrTiO_3$ substrates[18–20,35,37–39,42]). The sharp rocking curves about the 002-diffraction condition of the $BaTiO_3$ (Figure 1c) further demonstrate the high crystalline quality of the membrane films (average full-width at half-maximum (FWHM) of 0.06°, as compared to 0.04° for epitaxial films on $GdScO_3$), contrasting with the significantly lower quality of $BaTiO_3$ films grown directly on $SrTiO_3$/Si (001)[4–7] (dashed lines Figure 1d; minimum FWHM of 0.3°).

Taken together, this indicates that (1) the etching process is clean and the films are not structurally degraded in the transfer process, (2) the roughness of the films remains low, as cross-checked with atomic force microscopy (Figure S3, Supporting Information), and (3) the electrode and ferroelectric layers remain epitaxially coupled (to one another) in the transferred membranes, preventing complete lattice relaxation towards their respective bulk lattice parameters. The latter realization, in turn, opens-up an unexplored opportunity to control the ferroelectric layer by engineering the mechanical constraints imposed by the electrode layers. A simple model that considers the elastic balance between the two electrode and ferroelectric layers in a freestanding heterostructure[53] (Supporting Information), shows that the elastic compliances, lattice misfit u_{misfit}, and layer thickness ratio *z* can be used to tailor the strain in the ferroelectric layer, ϵ_{FE} (Figure 1d), whose sign is exclusively determined by u_{misfit}. Conversely, in the epitaxial films, the strain is dictated by the substrate (Figure S4, Supporting Information). In general, this strategy will be limited by the combination of electrode and ferroelectric layers that can be epitaxially grown without significant structural relaxation, as is the case for the $Ba_{1-y}Sr_yRuO_3$ and

$Ba_{1-x}Sr_xTiO_3$ layers used herein (Figure S5, Supporting Information). The stress σ imposed on the ferroelectric layer is controlled in our system by the strontium content (x in the ferroelectric layer and y in the electrode layers, see Supporting Information) – which determines the lattice and elastic parameters of the individual layers – and the thickness ratio z. This is illustrated in X-ray diffraction scans (Figure 1b), where the position of the 002-diffraction peak of the $BaTiO_3$ layer (x = 0) lies in the bulk position for a single-layer membrane (bottom scan, Figure 1b), is only slightly shifted to lower angles when using electrode layers with small u_{misfit} (y = 0.5) and can be further shifted by continuously increasing the thickness of the electrode layers with larger u_{misfit} (y = 1, z = 0.2-0.8).

Consequently, the room-temperature tetragonality (c/a lattice parameter ratio) of the $BaTiO_3$ can be finely tuned, as demonstrated by the evolution of the in-plane a and out-of-plane c lattice parameters of the $BaTiO_3$ membranes as a function of the thickness ratio z for electrode compositions y = 0.5 and 1 (Figure 1e) which was obtained from reciprocal space maps about the 103-diffraction condition of $BaTiO_3$ (Figure S6-S7, Supporting Information). The interlayer stress in the membranes provides finer structural control over the ferroelectric lattice than epitaxial strain on single-crystal substrates, which is limited to discrete strain values given by the lattice parameters of commercially available crystals. In the following, we test the role of this interlayer stress on the evolution of the electrical properties of capacitor devices fabricated on $Pt/Ti/SiO_2/Si$ (001) substrates after transfer (Figure 1f and Experimental Section), and the role of an external stress on capacitor devices fabricated on the growth substrate and transferred to indium-tin oxide (ITO)-coated PET (Figure 1g).

The Curie temperature (T_C) in bulk $BaTiO_3$ crystals occurs at ~120°C, but this temperature is shifted in epitaxial films due to biaxial strain[25] and can also be tuned with

strontium content.[26,54] In the released membranes (**Figure 2**a), the elastic misfit with the electrode layers can be used to continuously modulate the transition temperature using the three tuning parameters (*x*, *y*, *z*). A wide range of T_C values can be achieved and here we show a number of T_C isosurfaces in this design space extracted from the analytical expression for T_C as a function of *x*, *y*, and *z* derived in the Supporting Information (here shown for compressively strained $Ba_{1-x}Sr_xTiO_3$ membranes within the range x = 0-0.2 and y = 0.5-1, but similar effects for in-plane tensile strain can also be extracted). Using a thermodynamic model,[55,56] we can predict the temperature dependence of the ferroelectric polarization for all membrane varieties studied herein (Figure 2b). The critical temperatures are shown to be widely tunable by varying *x*, *y*, and *z* and compare well with our experimentally observed peaks in dielectric permittivity measured as a function of temperature (Figure 2c and Figure S8, Supporting Information). This suggests that the simple models of strain in the tri-layer membranes are adequate to understand the evolution of the strain state and that our understanding of how to control the strain state of the ferroelectric is accurate. We can, therefore, either increase or decrease the T_C of our $BaTiO_3$ epitaxial films grown on $GdScO_3$ (having a misfit strain of -1%) upon release from the substrate depending on the selection of the electrode material (*y*) and thickness (*z*), with T_C values scaling linearly with the measured *c*/*a* ratio for these membranes (Figure 2d); here showing control across ~350°C.

Having observed that the strain state and, therefore, the structure of the ferroelectric layer can be tuned in a deterministic fashion, this has other implications for ferroelectric properties. For instance, the tetragonal distortion (*c*/*a* ratio) also controls both the depth of the double-well potential and the energy barrier for polarization reversal; in essence the larger the *c*/*a* ratio is, the more stable the polarization and the larger the coercive field should be at room temperature. The

released membranes show changes of polarization and coercive field with respect to the as-grown epitaxial films (Figure S9-S10, Supporting Information) that correlate with their tetragonal distortion: as *c*/*a* is increased, the measured polarization goes up (**Figure 3**a). Furthermore, lower coercive fields for polarization reversal can be achieved by decreasing *c*/*a* (by increasing *x* or decreasing *y* and/or *z*), although this comes with the design tradeoff of a decrease in the remanent polarization (Figure 3b). These results provide a possible strategy to target low-voltage device operation using thin-film ferroelectrics and provide access to coercive fields that approach single-crystal limits and are some of the lowest reported for $BaTiO_3$ thin films. Indeed, we obtain coercive fields (voltages) as low as 12.8 kV cm^{-1} (128 mV) for $BaTiO_3$ membranes measured at 10 kHz (or 9 kV cm^{-1} (90 mV) when measured at 1 Hz; Figure 3c), thus approaching the highly pursued sub-100 mV threshold.[57] We notice, however, that the frequency (*f*) dependence of the coercive field (E_C) is highly dependent on the mechanical constraints imposed on the films: from a log-log plot (Figure 3c) we identify a linear dependence that allows us to fit our data to the Ishibashi and Orihara model for domain-growth-limited switching,[58] where $E_c \propto f^{\beta}$. The fitting reveals a decrease by a factor of 2 and 4 in the scaling exponent β, with respect to the epitaxial films, for membranes with y = 1 and 0.5, respectively. Lower β values indicate lower frequency dispersion of coercive fields which implies a higher domain-wall mobility.[59] Faster dynamics under *ac* fields can be obtained by reducing the inhomogeneities caused by structural defects or surface roughness in the films;[60] however, these membranes show comparable structure quality and surface morphology to the epitaxial films, thus suggesting that the change of dynamics is directly related to the substrate release.

To provide further insight into domain-wall dynamics and the switching kinetics of the films, we performed pulsed-electric-field measurements (Experimental Section) on $BaTiO_3$ films

(x = 0) with $SrRuO_3$ (y = 1) electrodes clamped to the substrate and in released membranes with different c/a ratios transferred to silicon substrates. From the polarization transients for an epitaxial, on-substrate film (Figure 3d) as well as released (0, 1, 0.8) (Figure 3e) and (0, 1, 0.2) (Figure S11, Supporting Information) membranes transferred to silicon substrates, we extract the characteristic switching times for polarization reversal t_0 obtained for the different amplitudes of the switching pulse as fit to the Kolmogorov-Avrami-Ishibashi (KAI) model[61] (Experimental Section) (Figure 3f). The on-substrate $BaTiO_3$ film shows t_0 = 17 ns for a voltage pulse of 1.9 V, whereas the released (0, 1, 0.8) membrane exhibits a t_0 = 5 ns and a similar value of switched polarization and for the (0, 1, 0.2) membrane t_0 = 3 ns, but the switched polarization is halved with respect to the epitaxial film (Figure S11, Supporting Information). While different circuit RC time constants for the three heterostructure variants can contribute to differences in the measured switching times, we find that after rescaling by RC (Experimental Section), the membranes on silicon still show faster switching times (higher switching speeds; right axis, Figure 3f), indicating that the switching times are intrinsically different and not exclusively determined by the electrode resistances. This result agrees with the observation of faster domain dynamics under *ac* fields shown above.

Further, from the switching time dependence on the pulse amplitude, we can obtain the activation field α from Merz's law,[62] $t_0 \propto exp\left(-\frac{\alpha}{E}\right)$, which results in values that are nearly 20% and 50% lower for the released (0, 1, 0.8) and (0, 1, 0.2) membranes, respectively (Figure 3f), implying that the domain walls require less energy to move after release from the substrate and reducing the elastic constraint (*i.e.*, by reducing electrode thickness). This observation, together with the evidence of modified domain dynamics, points to a lower energy switching pathway upon removal of the mechanical constraint of the growth substrate. In tetragonal

ferroelectrics, 180° polarization switching via two successive ferroelastic 90° switching steps has been shown to be energetically less costly than a direct 180° switching step in both simulations[63] and experiments.[64] Whereas substrate clamping in epitaxial films renders such 90° switching events too costly, in these membranes – which are only weakly bonded to the silicon substrate – the local strains generated by the 90° switching steps can be readily accommodated thus facilitating this lower-energy switching process. Thus, the tri-layer membrane strain engineering demonstrated herein allows one to decrease switching voltages, and the reduced mechanical constraints are shown to enable additional switching mechanisms that improve switching speeds while maintaining high-quality interfaces and supporting long-term cycling stability (>10^9 cycles before breakdown; Figure S12, Supporting Information).

Our capacitor devices can also be transferred to flexible substrates, which allows for strain tuning of properties by inducing uniaxial tensile or compressive strains upon bending (**Figure 4**a). Large susceptibilities can be obtained at temperatures near the phase transition, or when multiple microstructural phases coexist and small external stimuli (*e.g.*, stress) can easily tune the phase stability. Here, we use a (0.2, 0.5, 0.8) membrane, where the 20% strontium alloying of $BaTiO_3$ allows us to shift T_C closer to room temperature and also reduces the misfit strain with the $Ba_{0.5}Sr_{0.5}RuO_3$ electrodes to near zero. Thermodynamic calculations accounting for multiple single- and poly-domain structures (including tetragonal, orthorhombic, and rhombohedral phases) (Supporting Information), show that many of these structures are energetically close and the most stable phase can be tuned with a small uniaxial strain, here considered along the [010] tetragonal direction (Figure 4b). When transferred to silicon substrates, the (0.2, 0.5, 0.8) membranes show $T_C \approx 70$°C (Figure 2b-d), resulting in a large dielectric permittivity near room temperature, as well as decreased polarization and switching

voltage (Figure 3a,b). These membranes can also be transferred to flexible PET polymer substrates while maintaining high crystallinity and close-to-bulk lattice parameters (Figure 4c).

We therefore transferred capacitor devices to PET coated with conductive ITO (Figure 1g) to explore the ferroelectric (Figure 4d) and dielectric (Figure 4e) response as a function of substrate bending (curvature). The uniaxial strain applied to our capacitors can be estimated from the substrate curvature as $\epsilon = t_{PET}/2R$, where t_{PET} is the substrate thickness (125 μm) and R is the radius of curvature. Given that $t_{PET} >> t_{FE}$, strain gradient effects in the films can be neglected. We observe that as the membranes are bent in a concave fashion, the polarization increases and the hysteresis loop becomes more square while the dielectric permittivity decreases near zero bias; conversely, as they are bent in a convex fashion, the polarization decreases, the hysteresis loop becomes more slanted, and the dielectric permittivity increases. These results can be qualitatively described by our thermodynamic model where polydomain *c*/*a* phases are found most stable in the strain range within our experimental reach (Supporting Information). At zero strain, a predominantly *c* domain phase is expected and is indeed found. Compressive strain (convex bending) has little effect on the domain structure and favors the formation of a small fraction of a_1 domains (in-plane domains perpendicular to the strain direction) within the still predominantly *c* domain matrix, whereas tensile strain (concave bending) favors a_2 domains (parallel to the strain direction) and increases their volume fraction with increasing strain (Figure 5b and Figure S13, Supporting Information). The experimentally observed bending-induced dielectric tunability ($\Delta\varepsilon_{33} = \left(\varepsilon_{33}^{bent} - \varepsilon_{33}^{flat}\right)/\varepsilon_{33}^{flat}$) as a function of the substrate curvature R^{-1}, is found to change by nearly 90% and follows a trend similar to the tunability calculated from our thermodynamic model for low-strain values, within the ±0.1% strain range (Figure 4f). We note that the tunability values obtained experimentally (left axis, Figure 4f) exceed the calculated

values (right axis, Figure 4f) by a factor of at least two, likely indicative of additional coexisting phases not considered in the calculation, contributing to the enhancement of the dielectric response upon straining. The measured dielectric response also shows a saturation behavior above curvature values of ~0.1% strain, potentially indicating sliding/slipping of the capacitor structures under large bending curvatures, limiting the strain transmission in our experiment. While strategies for improved adhesion or clamping via microfabrication may be designed in order to increment the magnitude of the applied strain,[65] our experiment demonstrates the high strain sensitivity of the single-crystal capacitors pre-designed to show large susceptibility at room temperature, with dielectric tunability values comparable to those obtained on $Ba_{0.5}Sr_{0.5}TiO_3$ and $Ba_{0.67}Sr_{0.33}TiO_3$ films grown on mica for curvatures 5 and 10 times larger, respectively.[11,12]

In conclusion, we demonstrate that functionalities in heterostructured oxide nanomembranes can be designed by taking advantage of interlayer elastic interactions. We have shown that in $BaTiO_3$-based nanomembranes, transition temperatures and coercive voltages can be manipulated via structural control and therefore adapted to the desired functionality, and observe how modified switching dynamics after substrate release allow one to reach nanosecond switching times on films transferred to silicon. Ultimately, control over the membrane structure allows for the design of highly susceptible devices that display large sensitivity to external parameters, as we exemplified here for ferroelectric capacitors placed on flexible substrates displaying large dielectric tunability upon low-level straining induced by bending. The fabrication tools and strain-engineering strategies shown here should inspire future work transferring the well-known functionalities of perovskite oxides to semiconductor-based devices, or targeting new functions activated by strain not achievable by epitaxial growth. One could, for

example, design heterostructured devices with asymmetric elastic boundary conditions, thus inducing strain gradients and enhancing flexoelectric responses on chemically homogeneous materials, fabricate freestanding devices out of suspended ferroelectric membranes with giant electromechanical performance, or apply mechanical straining methods to study unexplored elasto-/flexo-caloric effects[66,67] in ferroelectric films.

Acknowledgements

The authors acknowledge Ekaterina Khestanova for fruitful discussions. D.P. acknowledges funding from the European Union's Horizon 2020 research and innovation programme under the Marie Skłodowska-Curie grant agreement No. 797123 and funding to the ICN2 provided by the CERCA programme / Generalitat de Catalunya and by the Severo Ochoa Centres of Excellence programme, funded by the Spanish Research Agency (AEI, grant no. SEV-2017-0706). E.P., A.Q., R.R., and L.W.M. acknowledge the support of the Intel Corp. as part of the FEINMAN Program. R.X. acknowledges support from U.S. Department of Energy, Office of Basic Energy Sciences, Division of Materials Sciences and Engineering, under contract no. DE-AC02-76SF00515, and partial support from Stanford Geballe Laboratory for Advanced Materials (GLAM) Postdoctoral Fellowship program. J.K. acknowledges support from the U.S. Department of Energy, Office of Science, Office of Basic Energy Sciences, Materials Sciences and Engineering Division under Contract No. DE-AC02-05-CH11231 (Materials Project program KC23MP) for the development of ferroic thin-film heterostructures. Y.J. acknowledges U.S. Department of Energy, Office of Science, Office of Basic Energy Sciences, under Award Number DE-SC-0012375 for the development of the $BaTiO_3$ membranes. G.V. acknowledges the support of the National Science Foundation under Grant DMR-1708615. Y.-L.H.

acknowledges support from the U.S. Department of Energy Advanced Manufacturing Office H.Y.H acknowledges support from the Air Force Office of Scientific Research (AFOSR) Hybrid Materials MURI under award FA9550-18-1-0480. R.R. acknowledges support from the SRC-ASCENT center, which is part of the SRC-DARPA JUMP program.

Experimental Section

Synthesis of epitaxial thin films and single-crystal membranes: All films were grown using pulsed-laser deposition using a KrF excimer laser (248 nm, LPX 300, Coherent). Typical heterostructures are of the form t_E nm $Ba_{1-y}Sr_yRuO_3$/100 nm $Ba_{1-x}Sr_xTiO_3$/t_E nm $Ba_{1-y}Sr_yRuO_3$/7 nm $La_{0.7}Sr_{0.3}MnO_3$ with t_E ranging from 0 to 40 nm, x fixed at either 0 or 0.2 and y fixed at 1 or 0.5; all heterostructures studied herein were grown on $GdScO_3$ (110) substrates (CrysTec GmbH). The $La_{0.7}Sr_{0.3}MnO_3$ and bottom $Ba_{0.5}Sr_{0.5}RuO_3$ growths were carried out at a heater temperature of 775°C in a dynamic oxygen pressure of 20 mTorr with a laser fluence of 1.9 J cm^{-2} and a laser repetition rate of 2 Hz. The bottom $SrRuO_3$ growth was deposited at 690°C in 100 mTorr oxygen pressure with a laser fluence of 1.3 J cm^{-2} and laser repetition of 15 Hz. The $Ba_{1-x}Sr_xTiO_3$ layers were grown at 600°C in 40 mTorr oxygen pressure with a laser fluence of 1.5 J cm^{-2} and a laser repetition rate of 2 Hz. The top electrode $Ba_{1-y}Sr_yRuO_3$ layers were grown at same laser conditions as the bottom-electrode layers but at a temperature of 600°C. All layers were grown from ceramic stoichiometric targets of the same chemistry as the films (Praxair). Following growth, samples were cooled to room temperature at 10°C min^{-1} in a static oxygen pressure of 700 Torr.

To release the films from the $GdScO_3$ substrates, a polypropylene carbonate (PPC) film (Sigma Aldrich) was placed on a polydimethylsiloxane (PDMS) stamp (Sylgard184 from Dow Corning) and the film surface was adhered to the PPC (Figure S1, Supporting Information). The samples were then placed in a 1 mol L^{-1} KI + 0.1% HCl solution and removed from it when the $La_{0.7}Sr_{0.3}MnO_3$ was fully dissolved, as ascertained by visual inspection. The freestanding films attached to the PPC polymer were then transferred to either 200 nm Pt/20 nm Ti/300 nm SiO_2/Si

(001) or indium-tin-oxide coated polyethylene terephthalate (PET, Sigma Aldrich). Additional details of the transfer process are provided in the Supporting Information.

Structural and surface characterization: X-ray diffraction studies, including 2θ-ω and rocking curve line scans about symmetrical reflections of the films and substrates, were collected with a Panalytical X'pert Pro3 diffractometer (copper $K_{\alpha 1}$, 1.540598 Å), using a hybrid 2-bounce primary monochromator on the incident beam side and a PIXcel3D position-sensitive detector. Pseudocubic in-plane and out-of-plane lattice parameters were obtained from reciprocal space mapping studies about asymmetrical reflections using the detector fast frame-based 1D mode. The offset angle ω for the membrane samples was obtained by averaging the peak ω value of the same reflection acquired at azimuthal angles of φ = 0° and φ = 180°. Surface topography was studied using an atomic force microscope (MFP-3D, Asylum Research). Scanning electron microscopy was performed using a Quanta 3D field-emission-gun (FEG) scanning electron microscope.

Dielectric and ferroelectric measurements: Electrical measurements were performed on circular capacitor structures, defined on the films using dry etching via Ar-ion milling. The patterned circular electrodes studied herein were 20-40 μm in diameter and were contacted with gold plated tungsten probe tips. For dielectric measurements, a small AC voltage (5 mV, 1-100 kHz) was applied between the microfabricated top electrode and the counter electrode and the capacitance $C = \varepsilon\varepsilon_0 A/t_{FE}$ was measured using an impedance analyzer (E4990A, Keysight Technologies). The capacitor area A used to extract the dielectric permittivity ε was measured and confirmed with atomic force microscopy. Room-temperature polarization-electric field hysteresis loops were measured at frequencies from 1-10,000 Hz using a Precision Multiferroic tester (Radiant Technologies). The coercive field E_c was extracted as $(|E_c^+| + |E_c^-|)/2$, where $|E_c^+|$

and $|E_c^-|$ are the positive and negative field values for which the polarization is zero, and the remanent polarization was extracted as $(|P_r^+| + |P_r^-|)/2$, where $|P_r^+|$ and $|P_r^-|$ are the positive and negative values of polarization obtained at zero electric field after corrections of the loops for any bias field $(|E_c^+| - |E_c^-|)/2$. At least three different capacitors were measured for each sample, their hysteresis loop parameters were averaged, and the error was taken as the standard deviation. Electrical measurements under bending conditions were performed by fixing the polymer substrate to a metal foil or a polycarbonate sheet curved by a home-made three-point bending rig.

Switching-transient measurements were performed by applying a sequence of three voltage pulses with a pulse generator (Berkeley Nucleonics BN 765) across a series combination of the ferroelectric capacitor and a resistor and measuring the time dependence of the current through an oscilloscope (schematics of the measurement can be found in Ref. [68]). The first pulse (with a fixed amplitude of -2V and duration of 1 μs) poles the ferroelectric in a well-defined state, the second pulse, of reversed polarity, switches the polarization, and the third pulse, identical to the second one and applied after a delay of 10 ns, measures the dielectric response in the absence of a switching event. The switching current transient is then revealed by subtracting the dielectric response from the switching response. RC times are extracted from the current transient (non-switching) of the third pulse. The oxide counter electrode is directly contacted in the as-grown film, while it is accessed through the less resistive platinum contact in the released films transferred to Pt-coated silicon. This yields a lower circuit RC time for the latter (~2 ns versus ~5 ns in the clamped film).

The polarization transients were fitted to the Kolmogorov-Avrami-Ishibashi (KAI) model for uniformly polarized ferroelectrics wherein,

$$\frac{\Delta P(t)}{2P} = 1 - exp\left[-\left(\frac{t}{t_0}\right)^n\right]$$

where t_0 is the characteristic switching time and n is the effective dimensionality. Our fittings yield n~2, consistent with a polarization reversal process with 2D domain wall propagation as the rate-limiting step.

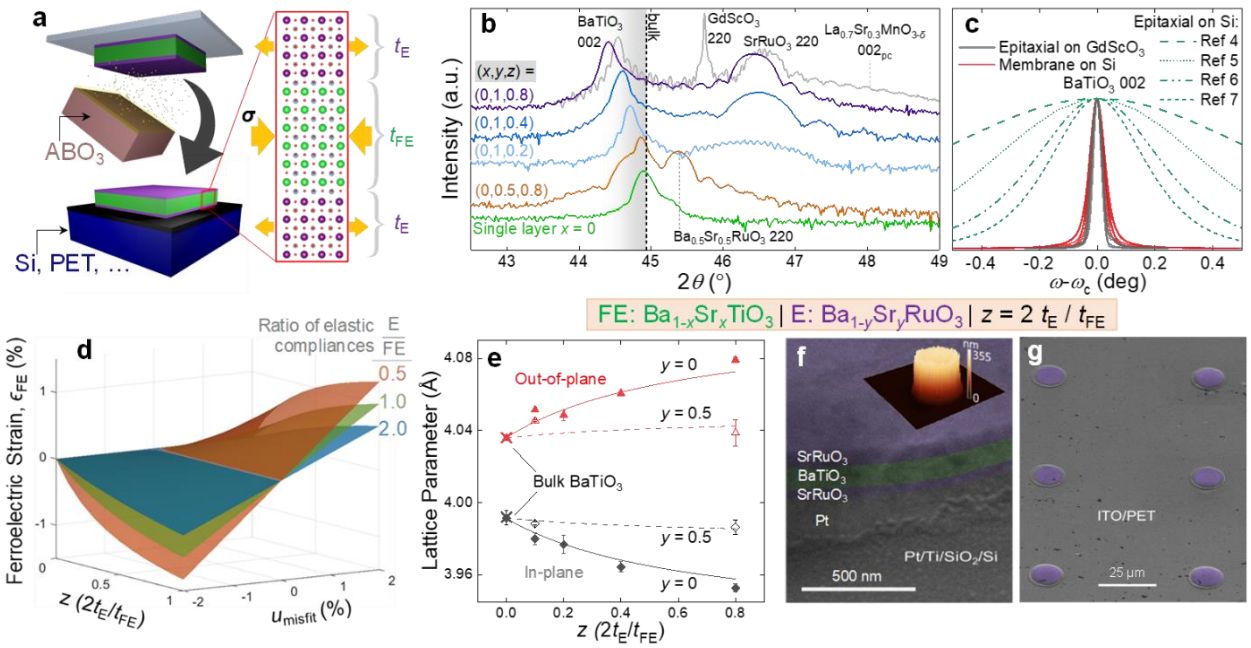

Figure 1. Fabrication and structural control of $BaTiO_3$ membranes and capacitor devices via elastic-boundary engineering. a) Membranes are fabricated via lift-off of an epitaxial heterostructure from a single-crystal oxide perovskite substrate by etching a sacrificial layer and subsequent transfer via polymer stamp onto an arbitrary substrate. After releasing the films from the substrate, the elastic balance between the electrode (E) and ferroelectric (FE) layers creates an internal stress σ. b) Top curves: θ-2θ scans about the $BaTiO_3$ 002-diffraction condition for a (x, y, z) = (0,1,0.8) tri-layer heterostructure before lift-off (grey) and after transfer to silicon (purple); the $BaTiO_3$ peak is shifted with respect to the single-layer membrane (bottom curve) with increasing y and z values in the tri-layer membranes on silicon. c) X-ray rocking curves about the 002-diffraction condition of all $BaTiO_3$ films, before lift-off (grey) and after transfer to silicon (red). Green dashed lines show different rocking curves found in the literature for $BaTiO_3$ films epitaxially grown on silicon. d) Calculations for the in-plane strain of a freestanding ferroelectric layer (FE) epitaxially constrained by two identical electrode layers (E) as a function of the in-plane lattice misfit (u_{misfit}), and layer-thickness ratio (z) for different ratios of elastic compliances (S_{11}+S_{12}) (Supporting Information). e) In-plane (grey diamonds) and out-of-plane

(red triangles) lattice parameters of the $BaTiO_3$ layers constrained by electrode layers of $SrRuO_3$ (filled symbols) and $Ba_{0.5}Sr_{0.5}RuO_3$ (open) as a function of thickness ratio *z*. Cross symbols indicate the lattice parameters of bulk $BaTiO_3$[25] and lines are calculations of the lattice parameters assuming elastic balance between layers, considering the bulk lattice parameters and elastic constants shown in Tables S1 and S2 (Supporting Information), and a $BaTiO_3$ Poisson's ratio of 0.35.[69] Scanning electron microscopy image of a capacitor fabricated on a tri-layer membrane on (f) a Pt/Ti/SiO_2/Si (001) substrate (wherein the inset is a 3D atomic force microscopy image of the capacitor) and (g) capacitors transferred to ITO coated PET.

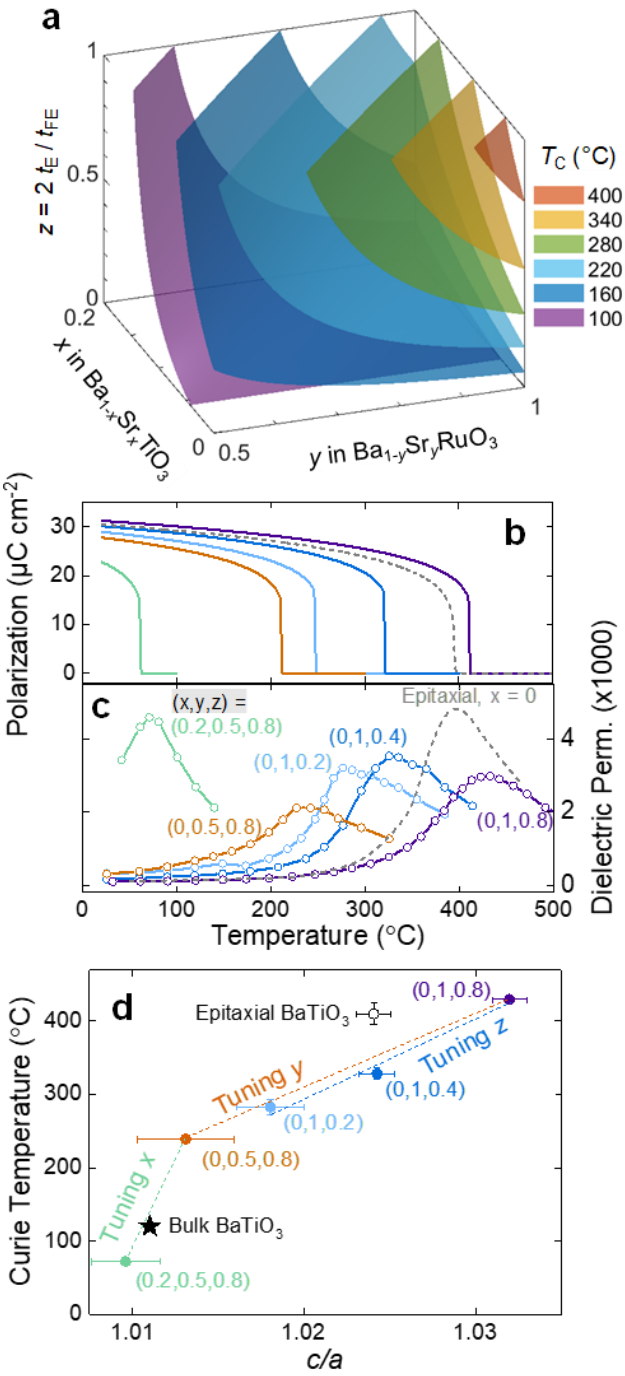

Figure 2. Engineering the Curie temperature of $Ba_{1-x}Sr_xTiO_3$ membranes on silicon. a) Calculated T_C isosurfaces of freestanding tri-layer heterostructures as a function of *x*, *y*, and *z* tuning parameters. b) Simulated temperature dependence of polarization. c) Measured temperature dependence of dielectric permittivity on capacitor devices of various (*x*, *y*, *z*) heterostructure types transferred onto silicon substrates. d) Curie temperature obtained from the

peak in permittivity in (c) (filled symbols) as a function of tetragonality in the ferroelectric layer, c/a. Dashed lines are guides to the eye, indicating the evolution of T_C when changing the tuning parameters x, y, and/or z. Transition temperatures obtained for the epitaxial $BaTiO_3$ samples grown on $GdScO_3$ (empty dot) and for bulk crystals[25] (star) are also shown.

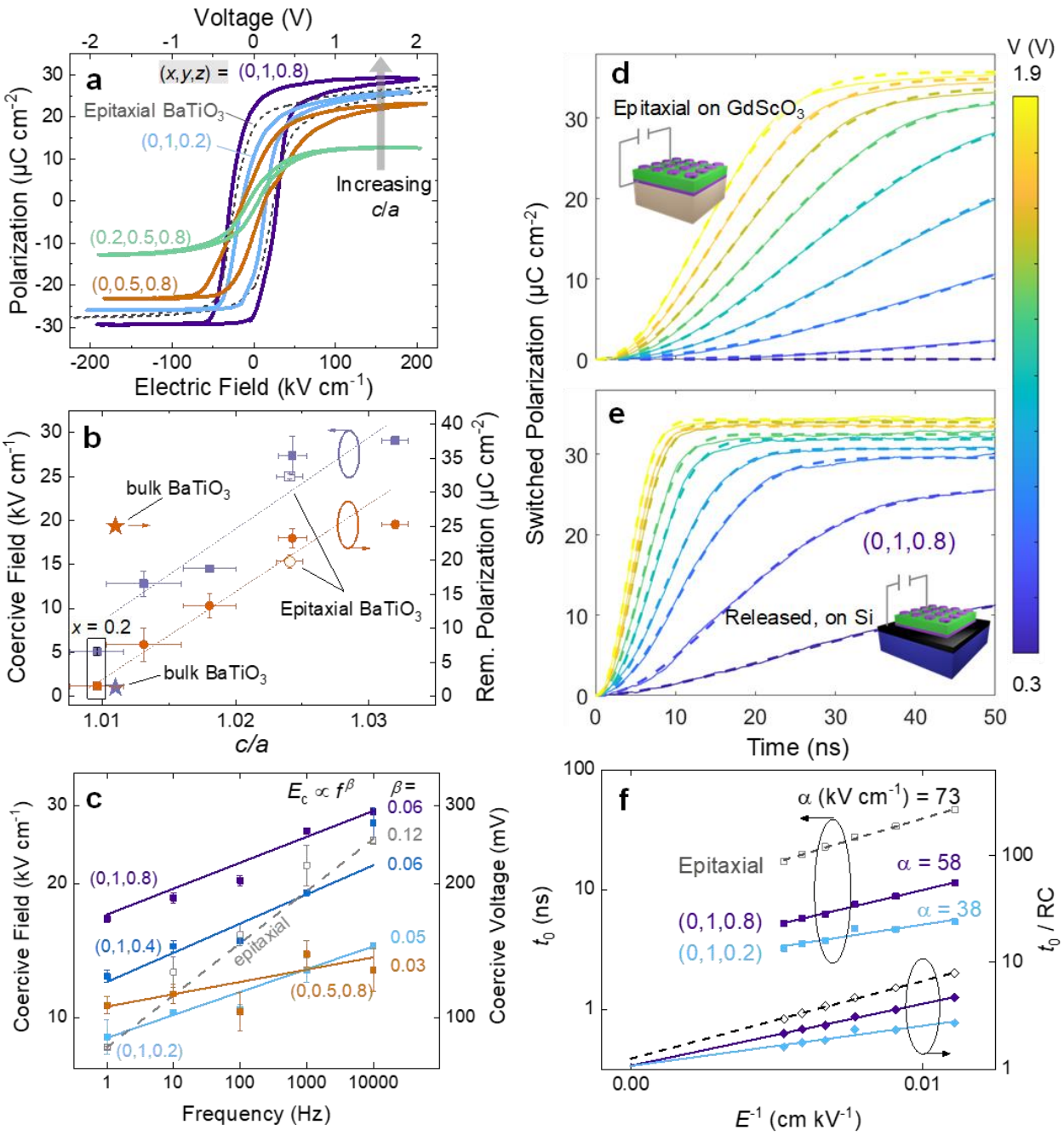

Figure 3. Controlling room temperature polarization and switching dynamics of $Ba_{1-x}Sr_xTiO_3$ membranes on silicon. a) Room temperature ferroelectric polarization hysteresis loops measured at a frequency of 10 kHz on capacitor devices of various (*x*, *y*, *z*) heterostructure types transferred onto silicon substrates. Data for an epitaxial $BaTiO_3$ sample with $SrRuO_3$ electrodes is also shown (dashed). Ferroelectric hysteresis loops are corrected for bias imprint and permittivity

contributions at high field. b) Coercive field (left axis) and remanent polarization (right axis) obtained from polarization hysteresis loops, as a function of *c*/*a*. Data for epitaxial samples on $GdScO_3$ substrates are shown as empty symbols and bulk $BaTiO_3$ data[25] is shown as star symbols. Lines are guides to the eye. c) Frequency dependence of the coercive field (log-log plot) obtained for all $BaTiO_3$ membranes (filled symbols) and epitaxial films (open symbols). Lines are fits to the Ishibashi and Orihara model. Switched polarization obtained from the integration of the current transient after a switching voltage pulse of varying amplitude, for an as-grown $BaTiO_3$ epitaxial film (with 10 nm $SrRuO_3$ electrodes) on (d) $GdScO_3$, and (e) a $BaTiO_3$ membrane on silicon with $SrRuO_3$ electrodes of thickness 40 nm (data for $BaTiO_3$ membrane 10 nm $SrRuO_3$ electrodes shown in Figure S11, Supporting Information). Dashed lines are fits to the KAI model. f) Polarization switching times as a function of the inverse of electric field pulse amplitude for three $BaTiO_3$ films, before (left axis) and after (right axis) rescaling with the circuit RC time. Lines are fits to Merz's law.

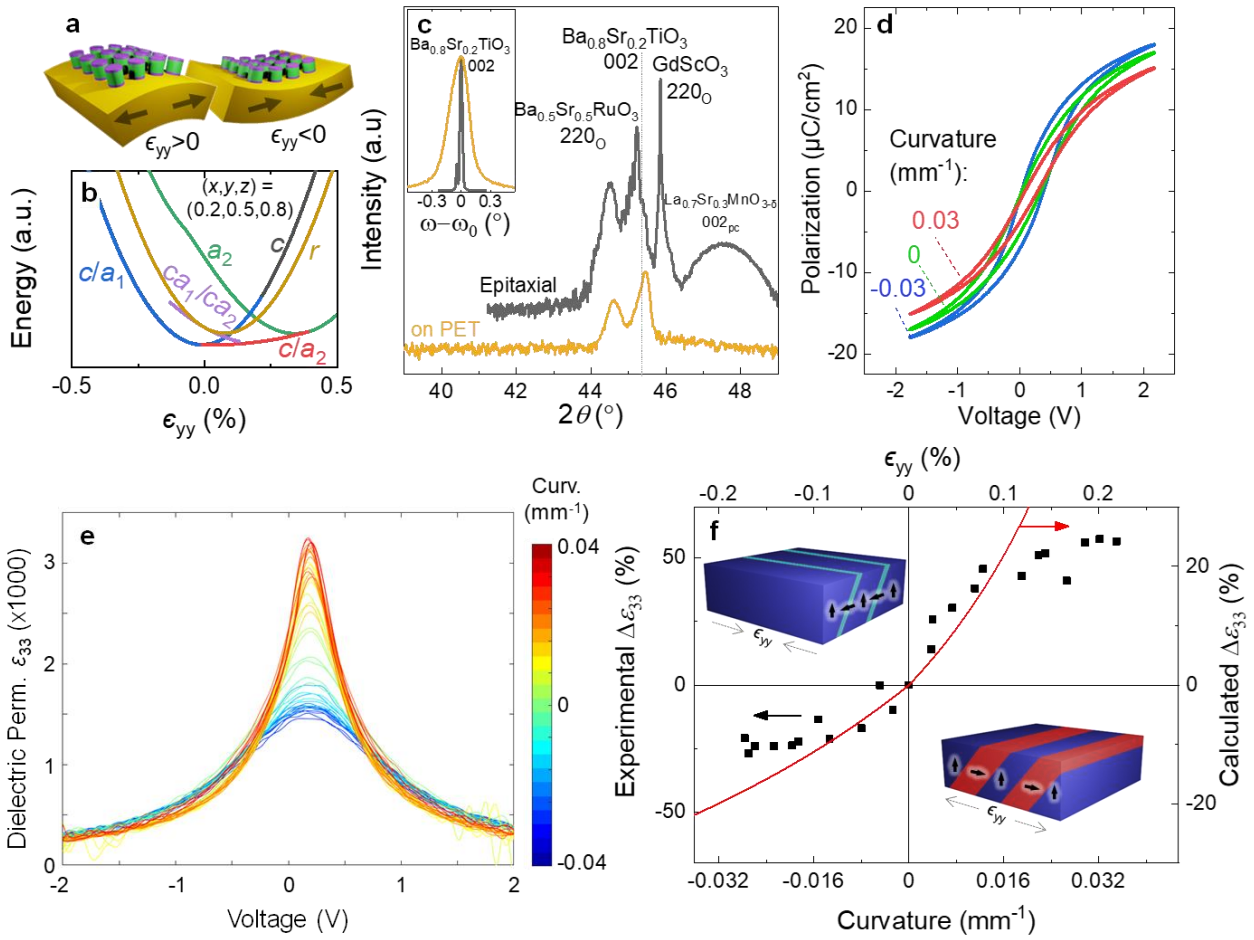

Figure 4. Strain manipulation of functional properties of $Ba_{0.8}Sr_{0.2}TiO_3$ membranes on flexible PET substrates. a) Capacitors transferred to a flexible PET substrate experience a uniaxial tensile (compressive) strain upon convex (concave) substrate bending. b) Calculated free energy density as a function of in-plane uniaxial strain for different domain configurations in a (0.2, 0.5, 0.8) membrane. c) θ-2θ scan (main panel) and rocking curve (inset) about the 002-diffraction condition of $Ba_{0.8}Sr_{0.2}TiO_3$ grown on $GdScO_3$ (grey) and transferred to PET (orange). d) Ferroelectric hysteresis loops measured at 10 kHz under different bending conditions on capacitor devices transferred to PET. e) Voltage dependence of dielectric permittivity measured at 10 kHz under different substrate curvatures. f) Measured (left axis) and calculated (right axis) bending-induced dielectric tunability as a function of substrate curvature (bottom) and estimated bending strain (top). Experimental data are obtained from the peak dielectric permittivity in (e);

red line shows the strain dependence obtained from a phenomenological poly-domain model; schematic drawings show the expected domain configurations from the model, for the largest strain values reached in the experiment (Figure S13, Supporting Information).

References

[1] R. A. McKee, F. J. Walker, M. F. Chisholm, *Phys. Rev. Lett.* **1998**, *81*, 3014.

[2] J. W. Reiner, A. M. Kolpak, Y. Segal, K. F. Garrity, S. Ismail-Beigi, C. H. Ahn, F. J. Walker, *Adv. Mater.* **2010**, *22*, 2919.

[3] S. H. Baek, J. Park, D. M. Kim, V. A. Aksyuk, R. R. Das, S. D. Bu, D. A. Felker, J. Lettieri, V. Vaithyanathan, S. S. N. Bharadwaja, N. Bassiri-Gharb, Y. B. Chen, H. P. Sun, C. M. Folkman, H. W. Jang, D. J. Kreft, S. K. Streiffer, R. Ramesh, X. Q. Pan, S. Trolier-McKinstry, D. G. Schlom, M. S. Rzchowski, R. H. Blick, C. B. Eom, *Science* **2011**, *334*, 958.

[4] L. Mazet, S. M. Yang, S. V. Kalinin, S. Schamm-Chardon, C. Dubourdieu, *Sci. Technol. Adv. Mater.* **2015**, *16*, 036005.

[5] M. Scigaj, C. H. Chao, J. Gázquez, I. Fina, R. Moalla, G. Saint-Girons, M. F. Chisholm, G. Herranz, J. Fontcuberta, R. Bachelet, F. Sánchez, *Appl. Phys. Lett.* **2016**, *109*, 122903.

[6] C. Xiong, W. H. P. Pernice, J. H. Ngai, J. W. Reiner, D. Kumah, F. J. Walker, C. H. Ahn, H. X. Tang, *Nano Lett.* **2014**, *14*, 1419.

[7] S. Abel, F. Eltes, J. E. Ortmann, A. Messner, P. Castera, T. Wagner, D. Urbonas, A. Rosa, A. M. Gutierrez, D. Tulli, P. Ma, B. Baeuerle, A. Josten, W. Heni, D. Caimi, L. Czornomaz, A. A. Demkov, J. Leuthold, P. Sanchis, J. Fompeyrine, *Nat. Mater.* **2019**, *18*, 42.

[8] Y.-H. Chu, *npj Quantum Mater.* **2017**, *2*, 67.

[9] T. Amrillah, Y. Bitla, K. Shin, T. Yang, Y. H. Hsieh, Y. Y. Chiou, H. J. Liu, T. H. Do, D. Su, Y. C. Chen, S. U. Jen, L. Q. Chen, K. H. Kim, J. Y. Juang, Y. H. Chu, *ACS Nano* **2017**, *11*, 6122.

[10] J. Jiang, Y. Bitla, C.-W. Huang, T. H. Do, H.-J. Liu, Y.-H. Hsieh, C.-H. Ma, C.-Y. Jang, Y.-H. Lai, P.-W. Chiu, W.-W. Wu, Y.-C. Chen, Y.-C. Zhou, Y.-H. Chu, *Sci. Adv.* **2017**, *3*, e1700121.

[11] D. L. Ko, M. F. Tsai, J. W. Chen, P. W. Shao, Y. Z. Tan, J. J. Wang, S. Z. Ho, Y. H. Lai, Y. L. Chueh, Y. C. Chen, D. P. Tsai, L.-Q. Chen, Y. H. Chu, *Sci. Adv.* **2020**, *6*, eaaz3180.

[12] D. Gao, Z. Tan, Z. Fan, M. Guo, Z. Hou, D. Chen, M. Qin, M. Zeng, G. Zhou, X. Gao, X. Lu, J. Liu, *ACS Appl. Mater. Interfaces* **2019**, *11*, 27088.

[13] A. K. Geim, I. V Grigorieva, *Nature* **2014**, *499*, 419.

[14] Y. Liu, Y. Huang, X. Duan, *Nature* **2019**, *567*, 323.

[15] F. Liu, W. Wu, Y. Bai, S. H. Chae, Q. Li, J. Wang, J. Hone, X.-Y. Zhu, *Science* **2020**, *367*, 903.

[16] D. M. Paskiewicz, R. Sichel-Tissot, E. Karapetrova, L. Stan, D. D. Fong, *Nano Lett.* **2016**, *16*, 534.

[17] S. R. Bakaul, C. R. Serrao, M. Lee, C. W. Yeung, A. Sarker, S.-L. Hsu, A. K. Yadav, L. Dedon, L. You, A. I. Khan, J. D. Clarkson, C. Hu, R. Ramesh, S. Salahuddin, *Nat. Commun.* **2016**, *7*, 10547.

[18] D. Lu, D. J. Baek, S. S. Hong, L. F. Kourkoutis, Y. Hikita, H. Y. Hwang, *Nat. Mater.* **2016**, *15*,

1255.

[19] P. Singh, A. Swartz, D. Lu, S. S. Hong, K. Lee, A. F. Marshall, K. Nishio, Y. Hikita, H. Y. Hwang, *ACS Appl. Electron. Mater.* **2019**, *1*, 1269.

[20] Z. Chen, B. Y. Wang, B. H. Goodge, D. Lu, S. S. Hong, D. Li, L. F. Kourkoutis, Y. Hikita, H. Y. Hwang, *Phys. Rev. Mater.* **2019**, *3*, 060801.

[21] H. S. Kum, H. Lee, S. Kim, S. Lindemann, W. Kong, K. Qiao, P. Chen, J. Irwin, J. H. Lee, S. Xie, S. Subramanian, J. Shim, S. Bae, C. Choi, L. Ranno, S. Seo, S. Lee, J. Bauer, H. Li, K. Lee, J. A. Robinson, C. A. Ross, D. G. Schlom, M. S. Rzchowski, C.-B. Eom, J. Kim, *Nature* **2020**, *578*, 75.

[22] M. A. Carpenter, *J. Phys. Condens. Matter* **2015**, *27*, 263201.

[23] A. R. Damodaran, J. C. Agar, S. Pandya, Z. Chen, L. Dedon, R. Xu, B. Apgar, S. Saremi, L. W. Martin, *J. Phys. Condens. Matter* **2016**, *28*, 263001.

[24] J. H. Haeni, P. Irvin, W. Chang, R. Uecker, P. Reiche, Y. L. Li, S. Choudhury, W. Tian, M. E. Hawley, B. Craigo, A. K. Tagantsev, X. Q. Pan, S. K. Streiffer, L. Q. Chen, S. W. Kirchoefer, J. Levy, D. G. Schlom, *Nature* **2004**, *430*, 758.

[25] K. J. Choi, M. Biegalski, Y. L. Li, A. Sharan, J. Schubert, R. Uecker, P. Reiche, Y. B. Chen, X. Q. Pan, V. Gopalan, L.-Q. Chen, D. G. Schlom, C. B. Eom, *Science* **2004**, *306*, 1005.

[26] Y. Dai, J. Schubert, E. Hollmann, G. Mussler, R. Wördenweber, *J. Appl. Phys.* **2016**, *120*, 114101.

[27] J. Karthik, J. C. Agar, A. R. Damodaran, L. W. Martin, *Phys. Rev. Lett.* **2012**, *109*, 257602.

[28] Y. H. Chu, Q. Zhan, L. W. Martin, M. P. Cruz, P. L. Yang, G. W. Pabst, F. Zavaliche, S. Y. Yang, J. X. Zhang, L. Q. Chen, D. G. Schlom, I. N. Lin, T. B. Wu, R. Ramesh, *Adv. Mater.* **2006**, *18*, 2307.

[29] S. Das, Y. L. Tang, Z. Hong, M. A. P. Gonçalves, M. R. McCarter, C. Klewe, K. X. Nguyen, F. Gómez-Ortiz, P. Shafer, E. Arenholz, V. A. Stoica, S.-L. Hsu, B. Wang, C. Ophus, J. F. Liu, C. T. Nelson, S. Saremi, B. Prasad, A. B. Mei, D. G. Schlom, J. Íñiguez, P. García-Fernández, D. A. Muller, L. Q. Chen, J. Junquera, L. W. Martin, R. Ramesh, *Nature* **2019**, *568*, 368.

[30] F. Weyland, M. Acosta, J. Koruza, P. Breckner, J. Rödel, N. Novak, *Adv. Funct. Mater.* **2016**, *26*, 7326.

[31] H. Fu, R. E. Cohen, *Nature* **2000**, *403*, 281.

[32] R. J. Zeches, M. D. Rossell, J. X. Zhang, A. J. Hatt, Q. He, C.-H. Yang, A. Kumar, C. H. Wang, A. Melville, C. Adamo, G. Sheng, Y.-H. Chu, J. F. Ihlefeld, R. Erni, C. Ederer, V. Gopalan, L. Q. Chen, D. G. Schlom, N. A. Spaldin, L. W. Martin, R. Ramesh, *Science* **2009**, *326*, 977.

[33] T. T. A. Lummen, Y. Gu, J. Wang, S. Lei, F. Xue, A. Kumar, A. T. Barnes, E. Barnes, S. Denev, A. Belianinov, M. Holt, A. N. Morozovska, S. V. Kalinin, L.-Q. Chen, V. Gopalan, *Nat. Commun.* **2014**, *5*, 3172.

[34] A. S. Everhardt, T. Denneulin, A. Grünebohm, Y.-T. Shao, P. Ondrejkovic, S. Zhou, N. Domingo, G. Catalan, J. Hlinka, J.-M. Zuo, S. Matzen, B. Noheda, *Appl. Phys. Rev.* **2020**, *7*, 011402.

[35] G. Dong, S. Li, M. Yao, Z. Zhou, Y. Zhang, X. Han, Z. Luo, J. Yao, B. Peng, Z. Hu, H. Huang, T. Jia, J. Li, W. Ren, Z. Ye, X. Ding, J. Sun, C. Nan, L. Chen, J. Li, M. Liu, *Science* **2019**, *366*, 475.

[36] H. Elangovan, M. Barzilay, S. Seremi, N. Cohen, Y. Jiang, L. W. Martin, Y. Ivry, *ACS Nano* **2020**, *14*, 5053.

[37] L. Han, Y. Fang, Y. Zhao, Y. Zang, Z. Gu, Y. Nie, X. Pan, *Adv. Mater. Interfaces* **2020**, *7*, 1901604.

[38] S. S. Hong, M. Gu, M. Verma, V. Harbola, B. Y. Wang, D. Lu, A. Vailionis, Y. Hikita, R. Pentcheva, J. M. Rondinelli, H. Y. Hwang, *Science* **2020**, *368*, 71.

[39] H. Wang, L. Shen, T. Duan, C. Ma, C. Cao, C. Jiang, X. Lu, H. Sun, M. Liu, *ACS Appl. Mater. Interfaces* **2019**, *11*, 22677.

[40] D. Pesquera, E. Khestanova, M. Ghidini, S. Zhang, A. P. Rooney, F. Maccherozzi, P. Riego, S. Farokhipoor, J. Kim, X. Moya, M. E. Vickers, N. A. Stelmashenko, S. J. Haigh, S. S. Dhesi, N. D. Mathur, *Manuscript submitted for publication* **2020**.

[41] S. R. Bakaul, C. R. Serrao, O. Lee, Z. Lu, A. Yadav, C. Carraro, R. Maboudian, R. Ramesh, S. Salahuddin, *Adv. Mater.* **2017**, *29*, 1605699.

[42] Z.-D. Luo, J. J. P. Peters, A. M. Sanchez, M. Alexe, *ACS Appl. Mater. Interfaces* **2019**, *11*, 23313.

[43] D. Lu, S. Crossley, R. Xu, Y. Hikita, H. Y. Hwang, *Nano Lett.* **2019**, *19*, 3999.

[44] V. Nagarajan, A. Roytburd, A. Stanishevsky, S. Prasertchoung, T. Zhao, L. Chen, J. Melngailis, O. Auciello, R. Ramesh, *Nat. Mater.* **2003**, *2*, 43.

[45] D. Su, Q. Meng, C. A. F. Vaz, M.-G. Han, Y. Segal, F. J. Walker, M. Sawicki, C. Broadbridge, C. H. Ahn, *Appl. Phys. Lett.* **2011**, *99*, 102902.

[46] S. R. Bakaul, J. Kim, S. Hong, M. J. Cherukara, T. Zhou, L. Stan, C. R. Serrao, S. Salahuddin, A. K. Petford-Long, D. D. Fong, M. V. Holt, *Adv. Mater.* **2020**, *32*, 1907036.

[47] J. F. Scott, C. A. Paz de Araujo, *Science* **1989**, *246*, 1400.

[48] A. Chanthbouala, A. Crassous, V. Garcia, K. Bouzehouane, S. Fusil, X. Moya, J. Allibe, B. Dlubak, J. Grollier, S. Xavier, C. Deranlot, A. Moshar, R. Proksch, N. D. Mathur, M. Bibes, A. Barthélémy, *Nat. Nanotechnol.* **2011**, *7*, 101.

[49] J. Li, C. Ge, J. Du, C. Wang, G. Yang, K. Jin, *Adv. Mater.* **2020**, *32*, 1905764.

[50] K. R. Poeppelmeier, M. E. Leonowicz, J. C. Scanlon, J. M. Longo, W. B. Yelon, *J. Solid State Chem.* **1982**, *45*, 71.

[51] F. L. Tang, M. Huang, W. J. Lu, W. Y. Yu, *Surf. Sci.* **2009**, *603*, 949.

[52] P. Orgiani, A. Y. Petrov, R. Ciancio, A. Galdi, L. Maritato, B. A. Davidson, *Appl. Phys. Lett.*

2012, *100*, 042404.

[53] P. M. Mooney, G. M. Cohen, J. O. Chu, C. E. Murray, *Appl. Phys. Lett.* **2004**, *84*, 1093.

[54] A. R. Damodaran, S. Pandya, Y. Qi, S.-L. Hsu, S. Liu, C. Nelson, A. Dasgupta, P. Ercius, C. Ophus, L. R. Dedon, J. C. Agar, H. Lu, J. Zhang, A. M. Minor, A. M. Rappe, L. W. Martin, *Nat. Commun.* **2017**, *8*, 14961.

[55] S. Prokhorenko, N. A. Pertsev, *J. Appl. Phys.* **2011**, *110*, 074116.

[56] J. Zhang, J. C. Agar, L. W. Martin, *J. Appl. Phys.* **2015**, *118*, 244101.

[57] N. A. Spaldin, R. Ramesh, *Nat. Mater.* **2019**, *18*, 203.

[58] Y. Ishibashi, H. Orihara, *Integr. Ferroelectr.* **1995**, *9*, 57.

[59] S. M. Yang, J. Y. Jo, T. H. Kim, J.-G. Yoon, T. K. Song, H. N. Lee, Z. Marton, S. Park, Y. Jo, T. W. Noh, *Phys. Rev. B* **2010**, *82*, 174125.

[60] Y. J. Shin, B. C. Jeon, S. M. Yang, I. Hwang, M. R. Cho, D. Sando, S. R. Lee, J.-G. Yoon, T. W. Noh, *Sci. Rep.* **2015**, *5*, 10485.

[61] Y. Ishibashi, Y. Takagi, *J. Phys. Soc. Jpn* **1971**, *31*, 506.

[62] W. J. Merz, *Phys. Rev.* **1954**, *95*, 690.

[63] B. Meyer, D. Vanderbilt, *Phys. Rev. B* **2002**, *65*, 104111.

[64] D. Pesquera, B. Casals, J. E. Thompson, G. F. Nataf, X. Moya, M. A. Carpenter, *APL Mater.* **2019**, *7*, 051109.

[65] H. J. Conley, B. Wang, J. I. Ziegler, R. F. Haglund, S. T. Pantelides, K. I. Bolotin, *Nano Lett.* **2013**, *13*, 3626.

[66] Y. Liu, I. C. Infante, X. Lou, L. Bellaiche, J. F. Scott, B. Dkhil, *Adv. Mater.* **2014**, *26*, 6132.

[67] H. Khassaf, T. Patel, R. J. Hebert, S. P. Alpay, *J. Appl. Phys.* **2018**, *123*, 024102.

[68] E. Parsonnet, Y.-L. Huang, T. Gosavi, Chia-Ching, Lin, A. Qualls, D. Nikonov, I. Young, J. Bokor, L. W. Martin, R. Ramesh, *Manuscript submitted for publication* **2020**.

[69] A. C. Dent, C. R. Bowen, R. Stevens, M. G. Cain, M. Stewart, *J. Eur. Ceram. Soc.* **2007**, *27*, 3739.